Optimizing the optical response of uniaxial cerium hexaboride films for high-temperature plasmonic applications

Andrea Ruiz-Perona [a,b], Thien Duc Ngo [a], David Hernández-Pinilla [c], Wataru Hayami [a], Tadaaki Nagao [a,b,*]

[a] International Center for Materials Nanoarchitectonics (MANA), National Institute for Materials Science (NIMS), Tsukuba, Ibaraki 305-0044, Japan

[b] Department of Condensed Matter Physics, Graduate School of Science, Hokkaido University, Sapporo 060-0810, Japan

[c] Departamento de Física de Materiales, Universidad Autónoma de Madrid, 28049, Madrid, Spain

ABSTRACT

Refractory materials with good optical properties are required for the development of novel high-temperature photonic and plasmonic photothermal applications. Whereas conventional coinage plasmonic materials have excellent metallic properties but low melting points, most refractory metals exhibit moderate metallic responses and oxidize easily in the atmosphere. Hence, in this study, cerium hexaboride (CeB_6) thin films are grown via electron-beam deposition on Si(100) and sapphire substrates. Epitaxial growth of this material is achieved under specific conditions, thus yielding high crystallinity and strong metallic polarizability within the infrared spectral region. The optical properties of CeB_6 improved significantly depending on the template substrate and growth conditions, achieving six times higher plasmonic figure-of-merit on R-sapphire compared with that on Si substrates. The high performance of CeB_6 films, as reflected by their superior plasmonic figures-of-merit particularly in the near-infrared region (1.0–2.0 μm) compared with conventional refractory materials, renders them highly promising candidates for photothermal and optoelectronic applications.

KEYWORDS: CeB_6, epitaxial growth, rare-earth hexaborides, plasmonics, high-temperature applications

INTRODUCTION

Metal borides are a group of materials which exhibit covalent-like behavior chemically as well as mechanically, and exhibit high electrical conductivity similar to metals.[1] Such characteristics are uncommon and therefore scientifically interesting. From an engineering perspective, this family of materials is investigated less compared with more common ceramics such as oxides and nitrides. Within the metal borides group, rare-earth hexaborides (RB_6) exhibit various interesting electronic and magnetic properties that have received increasing attention over the last decades.[2,3] Previous studies have focused primarily on their mechanical properties, such as film hardness and adhesion, tribological properties, and corrosion behavior, or thermodynamic properties, such as thermionic emission.[3] Other recent works explore the thermo-optical properties of boride materials at high temperatures for energy conversion applications[4] by surface engineering. The optical properties in the ultra-violet region have been studied for photodetection applications.[5] However, only a few studies have investigated their optoelectronic and plasmonic properties, in particular their optical response in the infrared (IR) region of the radiation spectrum. These properties arise from the complicated interaction between the lattice structure and electronic properties of RB_6. Consequently, both the mechanical and optical properties are affected significantly by the crystallographic structure of the boride phase.

Boron-rich metallic borides typically have extremely complex crystal structures. However, metal hexaboride compounds crystallize in a simple cubic CsCl structure (space group Pm-3m), where the rare-earth atoms are located at the vertex of the cube and the boron octahedra occupy the body-center position. In this configuration, each rare-earth atom is surrounded by eight boron octahedra. This metallic atom donates electrons to the charge-deficient boron sublattice. Theoretical calculations, which agree well with experimental data, indicate that two electrons are donated by metallic atoms,[6,7] thus resulting in divalent hexaboride semiconductors and trivalent hexaborides metallic.[8,9] For trivalent rare-hearth atoms such as La or Ce, the electrons provided to the B_6 network contribute to the metallic conductivity of the crystal, which causes its behavior to resemble that of a metallic material with covalent bonding between atoms. This metallic nature significantly affects its optical response. However, because of the strong directionality of covalent boron–boron bonds, rare-earth hexaboride films tend to grow in an amorphous manner as the atomic radius of the rare-earth metal decreases and the B/metal atomic ratio increases.[3] Crystal quality varies widely depending on the growth conditions, which significantly affects the material properties.

Recent studies demonstrated the potential use of rare-earth hexaborides for heat shielding[10] and photothermal applications owing to their good absorptive properties and plasmonic resonances in the near-infrared (NIR) to IR range.[11] The low work function and chemical stability of some RB_6, such as LaB_6, allow them to be used extensively in industry for applications such as high-brightness electron sources and photoemitters[12], as well as solar absorbers[4] and photodetectors[5] for high-temperature applications. These materials have demonstrated to achieve better performance than conventional materials by combining their remarkable properties with micro-fabrication and nano-manipulation techniques.[13] Among these hexaboride materials, cerium hexaboride (CeB_6) exhibits properties similar to those of LaB_6, such as a high melting point, extreme hardness, high chemical stability, and an unusually low work function. Additionally, compared with LaB_6, CeB_6 exhibits lower volatility, which renders its operating temperature higher and a longer lifetime.[14] In recent studies, CeB_6 was fabricated on MgO substrates via molecular beam epitaxy to investigate its magnetic properties.[15],[16] Other researchers propose to fabricate CeB_6 film on SiC substrates by sputtering deposition aiming to develop a new type of heterostructure photodetector[5]. Furthermore, CeB_6 grown by physical vapor deposition was investigated to analyze the field electron emission for transmission electron microscopy (TEM), scanning electron microscopy (SEM), flat-panel displays, and direct thermal-to-electrical power converters.[1,2,17] However, studies pertaining to the optical properties of CeB_6 are limited, and the plasmonic behavior of this material (as well as other hexaborides) remains unexplored.

The promising optical response of borides,[18] along with their high stability at high temperatures owing to their covalent nature, render RB_6 promising materials for use in high-temperature photothermal emitter applications.[19,20] However, the thermophotonic performance of the materials must be improved if they are to be used in large scale applications.

In this study, we fabricated high-crystallinity $CeB_6(100)$ thin films on Si(100) and sapphire substrates via electron-beam deposition. This study aims to correlate the optical response of the material with its crystalline structure. The dielectric function and optical response of the highly crystalline CeB_6 thin film in the 250–3500 nm range are obtained. This characterization demonstrates the potential of this material for high-temperature plasmonic applications in the NIR to far-IR spectral regions. The plasmonic response of CeB_6 reported herein indicates significantly better performance compared with most common refractory plasmonic materials such as Mo or W and comparable performance with reference plasmonic materials such as Al, which cannot withstand high temperatures.

EXPERIMENTAL SECTION

CeB_6 thin films were fabricated on p-type doped Si (0.5 mm thickness, 10 - 20 ohm·cm, Wakatec, Japan) substrates with (100) orientation and sapphire (0.3 mm thickness, Daico MFG, Japan) substrates oriented along the C- and R- crystallographic planes by electron-beam deposition. The deposition process was carried out while heating the substrates at temperatures ranging from 700 °C to 1100 °C. The temperature of the substrate was increased using a SiC radiative heater with a thermocouple located behind the substrate, calibrated previously with an estimated error between the nominal and the real temperature of about 20 °C. The base pressure of the camber was $\sim 1.0\times10^{-8}$ Pa. CeB_6 source powder material (99% purity) was manufactured by Furuuchi Chemicals (Japan). The deposition rate was monitored by a quartz oscillating monitor located next to the substrate, and the deposition rate was 1.9-2.1 Å/s. The native Si oxide was removed via flash heating at 1000 °C. The thickness of the deposited films was around 200 nm.

The crystallographic information of the films was obtained using X-ray diffraction (XRD, SmartLab, Rigaku, Japan) with Cu Kα radiation ($\lambda = 1.5425$ Å) in a θ-2θ configuration. The surface morphology of the films was examined using SEM (SU-4800, Hitachi High-Technologies, Japan). The atomic structure was analyzed by confocal Raman spectroscopy (WITec alpha300) under the illumination of a 532 nm laser source. Surface roughness was measured with an AFM-NanoFTIR (Neaspec, Neascope)

The phonon frequencies of CeB_6 were calculated using the Quantum ESPRESSO (QE) code,[21,22] based on the density functional theory (DFT) with plane waves and pseudopotentials. The ultrasoft pseudopotentials[23] of cerium and boron from the QE library were used.[24] The generalized gradient-approximation functional of Perdew, Burke, and Ernzerhof (PBE) was employed.[25] Energy cutoffs of 70 and 710 Ry for plane waves and electron density, respectively, were sufficient to achieve total-energy convergence. K-point sampling was implemented using the Monkhorst–Pack scheme.[26] An ($8 \times 8 \times 8$) mesh was used to calculate electronic structures.

Electron backscatter diffraction (EBSD) was performed using an SEM system (JSM 7001-F, Jeol) to obtain backscattered Kikuchi diffraction (BKD) patterns. The measurements were conducted at a sample tilt angle of 70° under an acceleration voltage of 12 kV. The dielectric permittivity was measured using a variable-angle spectroscopic ellipsometer (SE 850 DUV, SENTECH, Germany) in the wavelength range from UV to NIR (300–3500 nm) at three incident angles (60°, 65°, and 70°). All the data were analyzed using the SpectraRay/3 software package (Sentech). The experimental data were fitted using the Drude–Lorentz/Tauc–Lorentz combined model for all the fittings, and the best fit was determined based on the least-squares value.

The absorptivity spectrum was simulated using rigorous coupled-wave analysis (RCWA) implemented in the DiffractMOD software (Synopsys RSoft Photonics Device Tools). The electromagnetic field excitation was propagated parallel to the z-axis, with the incident electric field oscillating along the grating (x-axis).

RESULTS AND DISCUSSION

To investigate the crystal growth and material properties of CeB_6 films deposited at high temperature, CeB_6 thin films were fabricated on Si and sapphire (Al_2O_3) substrates. For high-temperature applications of CeB_6, sapphire substrates present apparent advantages over silicon. These advantages include higher temperature stability of sapphire compared with Si, where diffusion or melting occurs at the interface at temperatures above 800 °C. Additionally, the dielectric nature of Al_2O_3 suppresses electron transfer, thus resulting in an enhanced plasmonic figure-of-merit (FOM) compared with Si substrates.

The SEM surface images of the CeB_6 layers deposited at 1100 °C on Si(100) substrate (Fig. 1a), C-sapphire (Fig. 1b), and R-sapphire (Fig. 1c) show that the underneath substrate significantly affects the crystallinity degree of the films. The film deposited on Si presented typical cubic crystalline structures corresponding to the bcc lattice structure of CeB_6 (CaB_6 type lattice, space group Pm-3m [221]). It exhibits large crystallites (approximately 1 μm); however, large empty spaces appear between the crystallites. Another remarkable feature is that some of the crystallites show a 45° rotation in the azimuthal plane, which can be related to the void spaces between the crystallites in this sample. By contrast, the samples deposited on sapphire exhibited an extremely compact and uniform structure. The films grown on C-sapphire (Fig. 1b) presented triangular structures in addition to the usual cubic structures, which possibly correspond to crystallites with three (100)-equivalent facets, thus forming a relatively rough surface morphology. The detailed surface images of these structures are presented in Fig. S1. Meanwhile, the samples fabricated on R-sapphire (Fig. 1c) showed compact rectangular/cubic structures, with approximately the same size as the film deposited on Si but without empty spaces between the crystallites. The samples deposited at 800 °C (Fig. 1d, e, f) showed a compact and crystalline structure on Si; however, the films appeared disconnected when deposited on sapphire, thus causing the film to charge electrically and resulting in unclear and unfocused SEM images. In addition, the crystallite size of the films deposited at 800 °C are much smaller than those deposited at 1100 °C, as can be clearly noted from the scales. The orientation of the crystallites resembles the samples deposited at 1100 °C, presenting cubic structures on Si and R-sapphire, and less-defined as well as triangular shapes when deposited on C-sapphire.

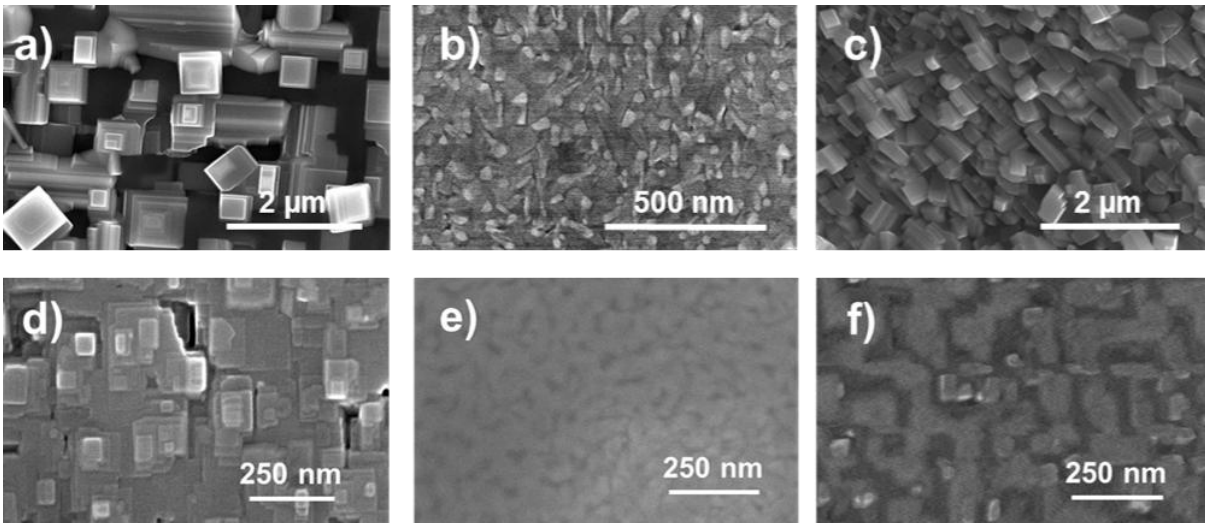

Fig. 1: Top SEM images of CeB_6 films deposited at 1100 °C on Si(100) (a), C-sapphire (b), and R-sapphire (c), and at 800 °C on Si(100) (d), C-sapphire (e), and R-sapphire (f).

The AFM mapping in Fig. 2 shows similar surface morphology to the one observed in the SEM images (Fig. 1). The films deposited on Si present big crystallites with a large step size (250 nm) in the height profile. On the other hand, the films deposited on sapphire exhibit a smaller crystallite size and a compact surface, presenting step sizes smaller than 25 nm on the height profiles. The surface roughness (R_{ms}) of the CeB_6 films is 57.6 nm, 2.2 nm and 1.9 nm for the films deposited on Si, C-sapphire and R-sapphire substrates respectively.

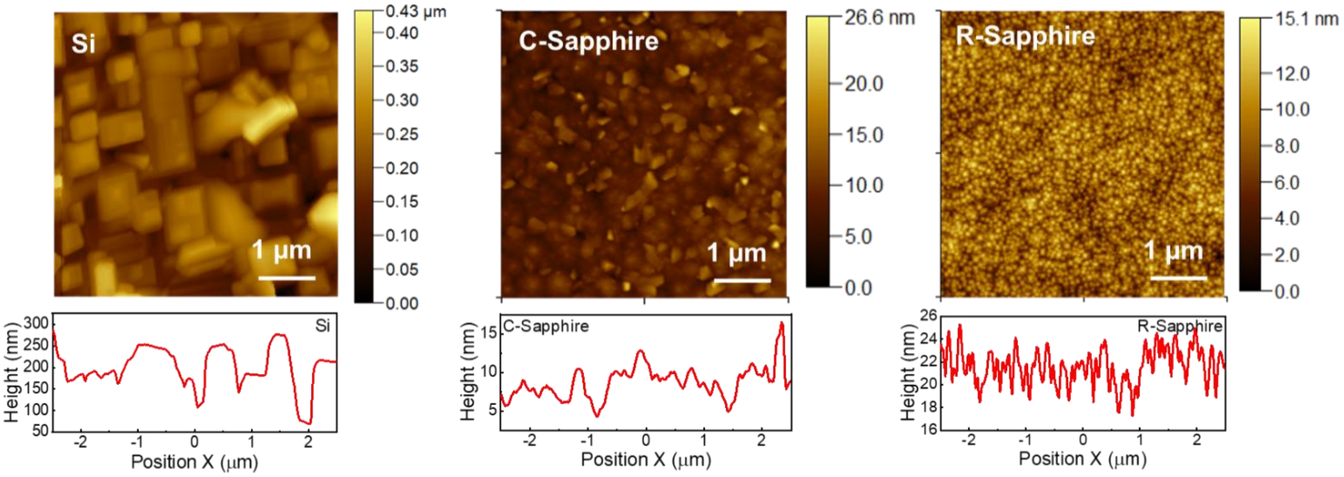

Fig. 2: Atomic Force Microscope imaging of the CeB_6 layers deposited on Si, C-sapphire and R-sapphire.

Fig. 3 shows the XRD pattern of the CeB_6 layers deposited on Si and sapphire at 800 °C and 1100 °C and a CeB_6 reference diffraction pattern.[27] At 800 °C, the films deposited on Si and R-sapphire presented unidirectional growth in the (100)–same as (200)–orientation with strong diffraction peaks at 21.4° and 43.6°, which corresponds to a cubic structure with lattice constant of 4.14 Å. However, in the sample deposited on C-sapphire, the main diffraction peak appeared at 37.6° and corresponded to the (111) orientation. Additionally, a peak corresponding to the C-sapphire substrate was observed at 42°. At a higher temperature (1100 ºC), in addition to the (100)-orientation diffraction peaks, a peak corresponding to the (110) orientation appeared at 30.6° for the film deposited on the Si substrate. The growth orientation of the films was determined to minimize their total energy. The orientation plane of the film parallel to the substrate is the result of the surface, strain, and interfacial energies combined. Increasing the growth temperature reduces the effects of anisotropy on the surface energy. Consequently, other energies, such as the strain energy due to thermal expansion mismatch, can become more important, and crystallographic planes other than those with the lowest surface energy can emerge in the structure.[28] The sample deposited on C-sapphire did not exhibit a peak corresponding to the (110) orientation; instead, a diffraction peak arising from the (111) orientation appeared at 37.6°. This orientation exhibits three-fold symmetry, which explains the triangular faceted structures observed in the SEM (Figs. 1 (b) and S1(b,b')) and AFM images (Fig. 2). The CeB_6 films grown at 1100 °C on R-sapphire presented only two diffraction peaks, which corresponded to (100) and (200) orientations, in addition to diffraction peaks arising from the R-sapphire substrate at 25.6° and 52.6°. These results show that the crystal orientation of the CeB_6 layers is strongly determined by the substrate. At low temperatures, CeB_6 can grow unidirectionally in the (100) orientation when deposited on Si substrates; however, to achieve epitaxial growth at higher temperatures (above 1000 ºC), and thus higher crystallinity, the substrate must be replaced by sapphire. Fig. 3c) shows the Full Width Half

Maxima (FWHM) of the main peaks of each diffractogram. Samples deposited at 800 ºC exhibit higher FWHM when deposited on C- and R-sapphire, indicating that the crystallinity decreases. However, for samples deposited at 1100 ºC, the FWHM is much lower for samples grown on R-sapphire, demonstrating a higher degree of crystallinity.

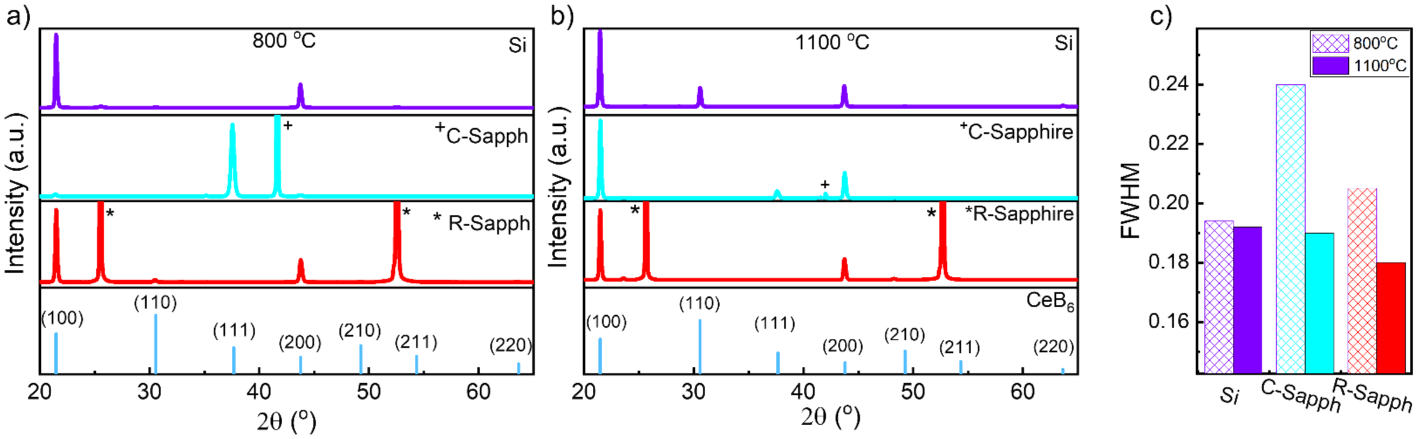

Fig. 3: X-ray diffraction spectra of CeB$_6$ deposited at 800 °C (a) and 1100 °C (b) on Si (purple), C-sapphire (blue), and R-sapphire (red). Reference CeB$_6$ XRD spectra from reference [27]. (c) Comparison of the Full Width Half Maxima (FWHM) of the main peaks of each diffractogram: (100) for all the samples, except for C-Sapphire 800 °C (111).

Fig. 4 shows the Raman-spectroscopy measurements of the films deposited on Si and sapphire at 800 °C and 1100 °C. The bulk Raman active vibrational modes of CeB$_6$ are the E$_g$ (1142 cm^{-1}) and A$_{1g}$ (1270 cm^{-1}) stretching modes and the T$_{2g}$ (680 cm^{-1}) bending mode[29] arising from inter- and intra-octahedral B-B bonds, respectively, and the T$_{1u}$ mode originating from the vibration of Ce inside the boron cage.[30–32] A small Raman peak corresponding to the Si substrate was observed at 520.7 cm^{-1}. The peaks at 450 cm^{-1} correspond to sapphire. The A$_{1g}$ (and E$_g$) Raman peaks shifted to lower energies (redshift) compared with those of the bulk CeB$_6$ single crystal (dashed line, 1270 cm^{-1}). The CeB$_6$ samples deposited on sapphire presented a larger redshift compared with the CeB$_6$ single crystal[29] than the samples deposited on Si. Peak shifting can originate from tensile or compressive strain within the film. In this case, a peak shift to lower energies indicates tensile stress, which implies that the lattice was subjected to expansion. However, Raman peak shifting can be related to other factors, such as charge transfer between the substrate and the film, self-doping by crystal defects, and/or chemical composition.[32–34] For instance, non-stoichiometric CeB$_6$ films with a cesium deficit present larger lattice parameters[35] owing to the internal stress on the film, which can result in a redshift in the Raman resonant phonon frequency. Lattice shrinking occurs in B-deficient films, thus inducing a peak shift to higher energies.[36] The stronger redshift at higher temperatures (as shown in Fig. 4) suggests that chemical variations might occur within the sample because of the excess thermal energy in the atoms, which can migrate either between the film and substrate or re-evaporate from the film surface.

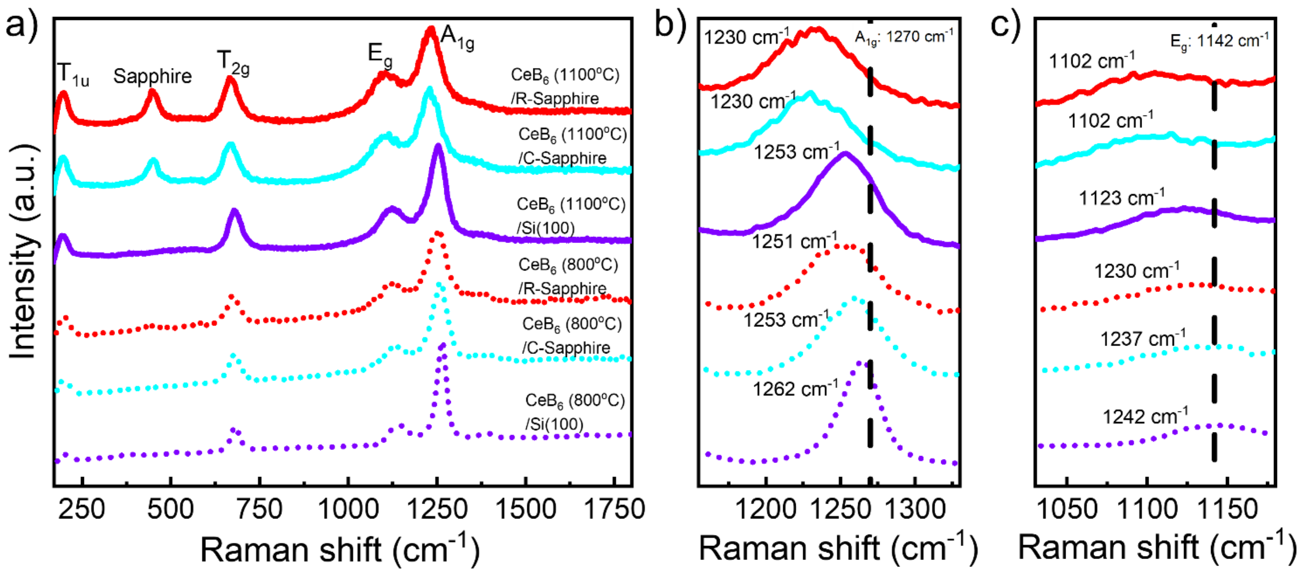

Fig. 4: (a) Raman scattering spectroscopy spectra of CeB_6 films deposited at 1100 °C on R-sapphire (red), C-sapphire (blue), and Si (purple) and at 800 °C on R-sapphire (dotted red), C-sapphire (dotted blue), and Si (dotted purple). b) A_{1g} Raman peak shifts compared with bulk resonant peak (dashed line). c) E_g Raman peak shifts compared with bulk resonant peak (dashed line).

To gain further insights into the lattice softening of the CeB_6 films deposited on different substrates, DFT calculations of the CeB_6 phonon vibration were performed. Fig. 5 shows the phonon vibrational frequencies of modes A_{1g} and E_g as a function of lattice expansion. Based on the Raman spectroscopy data presented above (Fig. 4), the Raman vibrational energy of peak A_{1g} at 1230 cm^{-1} (CeB_6 deposited on sapphire at 1100 ºC) corresponds to a 1.2% expansion, and that of 1263 cm^{-1} (CeB_6 deposited on Si at 800 ºC) corresponds to a 0.7% lattice expansion. These calculations are consistent with previous experimental results reported by Ishii[31] and Ogita.[30] Furthermore, an analysis of the thin-film XRD results indicates lattice expansions in the same order. However, the expansion of CeB_6 on sapphire grown at 1100 °C is smaller (0.3%) than the value expected from Raman spectroscopy, and the expansion of the films on Si(100) grown at 800 °C is larger (0.57%). The former phenomenon is attributable to the extremely high growth temperatures (maximum of 1100 °C), which may render the CeB_6 stoichiometry boron rich, as is allowed based on its phase diagram. Meanwhile, the latter might be caused by charge transfer from the CeB_6 film to the Si substrate. Additionally, diffusion at the interface between CeB_6 and Si can occur at high temperatures due to surface melting and atom rearrangement on the Si substrate at temperatures above 800 °C. Our calculations provide information regarding the Raman resonant peak shift when charge transfer occurs between the CeB_6 (work function, 2.4–2.6 eV) layer and Si (work function, 4.6–4.8 eV) substrate. This information may explain the smaller Raman peak shift from the bulk value on Si compared with that on sapphire. A charge transfer of 0.1 electron per unit cell increases the A_{1g} frequency by approximately 18 cm^{-1}, as opposed to the frequency decrease due to lattice expansion observed from the XRD pattern. Charge migration from CeB_6 to Si results in an electron deficit on the CeB_6 lattice, thus causing the CeB_6 structure to exhibit a slightly semiconductor nature. This strengthens the bonds in the lattice, thereby increasing the phonon vibrational frequency, as opposed the bond softening due to lattice expansion. The combined effect of lattice expansion and charge transfer can decrease the A_{1g} mode frequency by approximately 22 cm^{-1}, which agrees well with the experimental Raman measurements. Compared with Si, sapphire is an insulating dielectric material with a high electron work function, which implies that charge transfer from the CeB_6 layer is negligible. Therefore, the bond softening observed by Raman spectroscopy is solely associated with the stoichiometry change from the original CeB_6 during the high-temperature crystal growth (with a maximum temperature of 1100 °C).

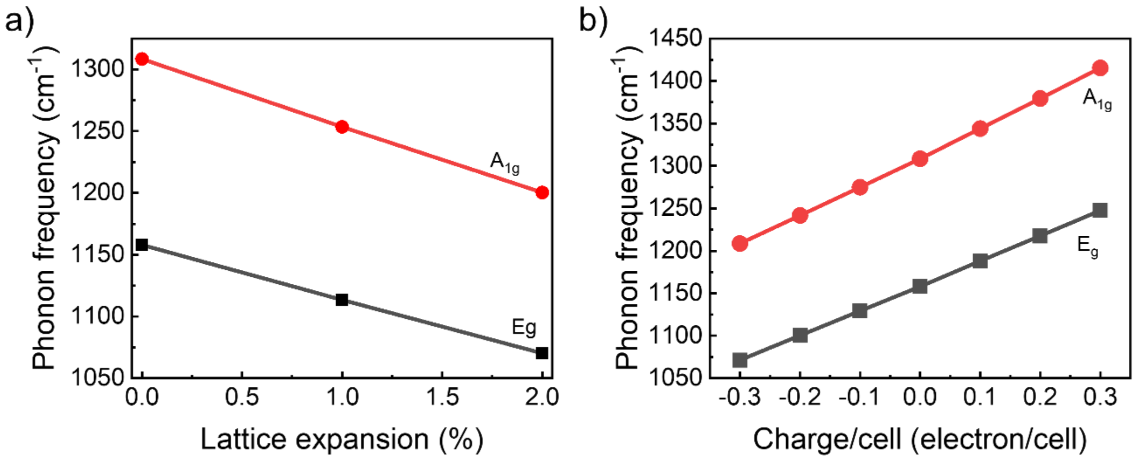

Fig. 5: Phonon frequency calculations of A_{1g} and E_g vibrational modes of CeB_6 for different lattice expansion parameters (a) and charge transfer (b) under isotropic expansion.

Regarding the lattice expansion, for the CeB_6 films deposited on R-sapphire substrates, the nearly commensurate lattice matching agreed well with supercell structures comprising 11 unit cells of CeB_6 and 3 unit cells of R-sapphire in the $[1\bar{1}01]$ direction. Similarly, a ratio of 8:7 for the unit cells was indicated in the $[11\bar{2}0]$ direction (Eq. S1). The small lattice mismatch between the sapphire substrate and overlayer may thrust the epitaxial growth of the CeB_6 film, thus enhancing the crystallinity of the material, which significantly affect the electro-optical properties. The growth mechanism can be further analyzed to understand the optimal conditions for achieving perfect epitaxial film growth.

To confirm the epitaxial growth of the CeB_6 layers, EBSD measurements were performed on the 1100 °C deposited sample. The Kikuchi patterns of the substrate and overlayer are shown in Fig. 6. The clear features presented in the obtained Kikuchi patterns show that the CeB_6 layer fabricated at 1100 °C is unidirectionally oriented, and the analysis of the EBSD Kikuchi pattern confirms that the orientation corresponds to the (100) direction. These characterizations suggest that the epitaxial growth of CeB_6 is enhanced by the lattice matching between the R-sapphire substrate and CeB_6(100) layer, which is analogous to previous reports regarding the LaB_6 growth process,[37] owing to the similar lattice parameters of LaB_6 and CeB_6 (4.157 and

4.142 nm, respectively).[38,39] Moreover, this epitaxial growth can be favored by the covalent bonding nature of CeB_6 films to sapphire[40] because covalent bonding promotes highly directional growth aligned to the substrate crystallographic orientation.[41,42]

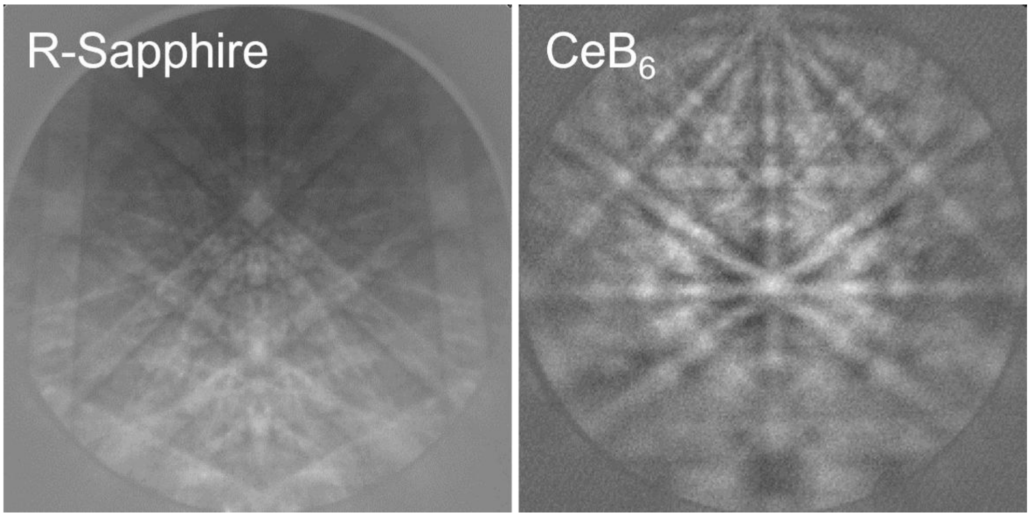

Fig. 6: Kikuchi patterns obtained by electron backscattered diffraction of sapphire substrate and CeB_6 films deposited on sapphire.

To evaluate the optical properties of the CeB_6 films, their dielectric permittivities (ε_1 and ε_2) were measured via spectroscopic ellipsometry (Fig. 7). The experimental data were fitted using a combination of the Drude–Lorentz/Tauc–Lorentz combined model, which is required to encompass all the different excitation modes that occur in this material. The Drude term, which is dominant in the IR spectral range, generally describes intraband electronic transitions, whereas interband electronic transitions are described by the Tauc–Lorentz term. More details can be found in the supporting information (Table S1).

The real part of the dielectric permittivity (ε_1) in Fig. 7a) shows that the films behave as dielectric materials in the UV–vis region ($\varepsilon_1 > 0$) and exhibit strong metallicity in the NIR and mid-infrared region ($\varepsilon_1 < 0$). In all the cases, the crossover point ($\varepsilon_1 = 0$) occurs between 622 and 740 nm. The metallicity of the samples decreases with increasing deposition temperature indicating decreased carrier mobility, in agreement with the electrical measurements (Fig. S2). The imaginary part of the complex permittivity (ε_2) of the films decreases when increasing temperature, which indicates a reduction in the optical losses of the material at higher temperatures. Fig. 7 b) demonstrates clear differences in the optical properties of samples grown on Si and sapphire, showing that samples fabricated on Si present lower optical losses, as well as lower metallicity. The calculation of the plasmonic figure of merit (FOM) is required to better understand the effect of these two opposite factors on the overall optical performance. Supplementary data can be found in Fig. S3.

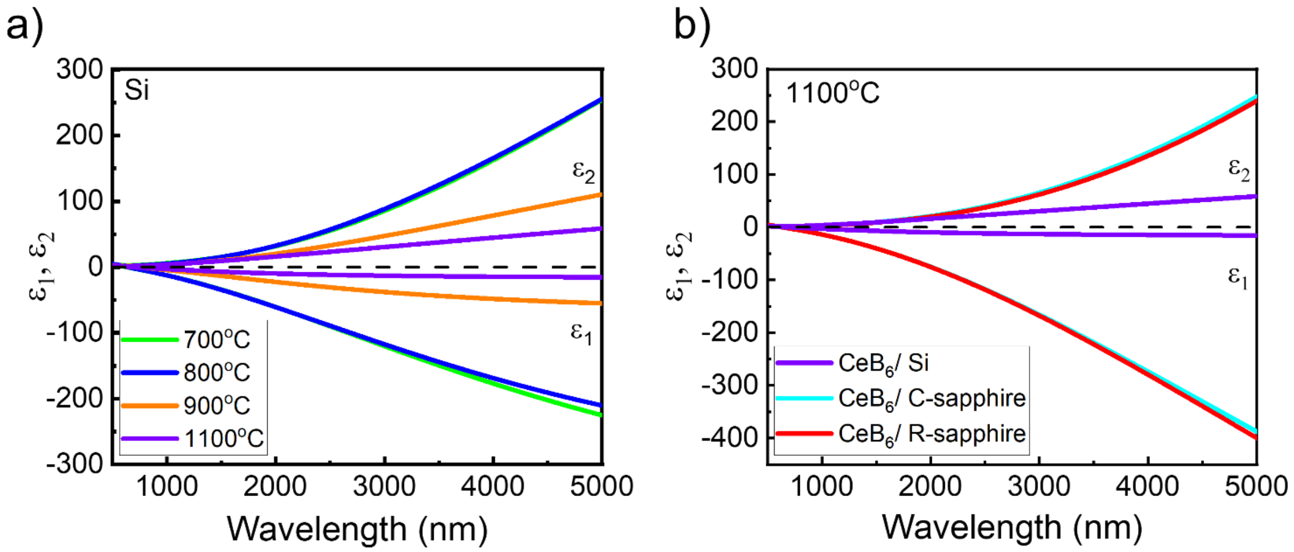

Fig. 7: Dielectric constants of the CeB_6 films deposited at different temperatures. (b) Comparison of the films deposited at 1100 °C on different substrates.

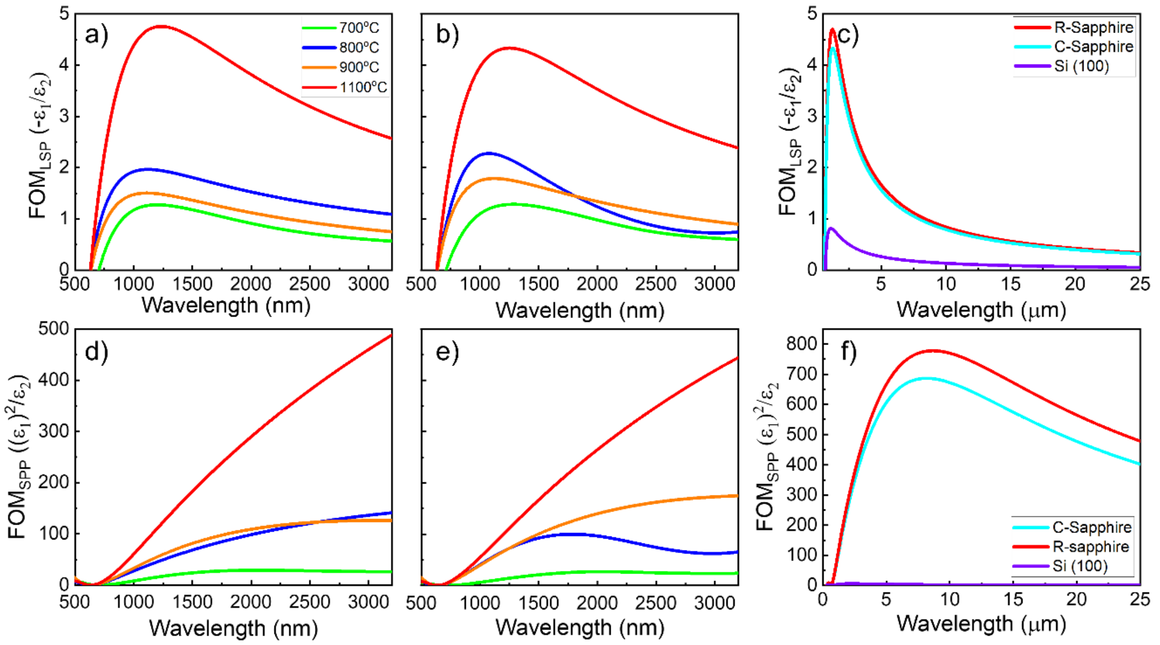

Fig. 8: Localized surface plasmon-based figure-of-merit (FOM_{LSP}), defined as $-\varepsilon_1/\varepsilon_2$ of samples deposited between 700 °C and 1100 °C on R-sapphire (a) and C-sapphire (b). (c) Comparison between FOM of CeB_6 thin films deposited at 1100 °C on different substrates. Surface plasmon polariton-based figure of merit (FOM_{SPP}), defined as $(\varepsilon_1)^2/\varepsilon_2$ of samples deposited between 700 °C and 1100 °C on R-sapphire (d) and C-sapphire (e). (

f) Comparison between FOM of CeB_6 thin films deposited at 1100 °C on different substrates.

The plasmonic FOM allows one to assess the overall optical performance of different samples and depends on the dielectric properties of the metal as well as the device structure geometry. The localized surface plasmon (LSP) figure-of-merit (FOM_{LSP}), which is defined as $-\varepsilon_1/\varepsilon_2$, is used for LSP based geometries (MIM devices), whereas the surface plasmon-polariton (SPP) figure-of-merit (FOM_{SPP}), which is defined as $(\varepsilon_1)^2/\varepsilon_2$, is applied to SPP-based geometries, such as grating or waveguide devices. Fig. 8 shows the plasmonic FOM of the films deposited on C- and R-sapphire at different temperatures (for films deposited on Si, see Fig. S4). The FOM of CeB_6 increased with the growth temperature. The films deposited at higher temperatures were smoother, more compact (denser), and presented a higher degree of crystallinity, which reduced the number of defects and electron scattering, thus resulting in better optical response, i.e., higher surface polarizability and lower Ohmic loss. The film deposited at 1100 °C presented the highest FOM_{LSP} in both cases, reaching values of 4.75 and 4.33 for R-sapphire and C-sapphire, respectively, which were more than twice that achieved at lower temperatures. This can be attributed to the better crystallization of metal hexaborides at temperatures above 1000 °C, as similarly reported for LaB_6.[19,20] The FOM_{SPP} showed a similar behavior, where higher values were achieved for the samples deposited at 1100 °C. In Figs. 8 c) and f), a comparison between the FOM of CeB_6 deposited at 1100 °C on different substrates are shown. The FOM_{LSP} of the film deposited on R-sapphire was more than six times larger than that of the film deposited on the Si substrate. This is attributable to the decreased electron mobility through the layer deposited on Si owing to the large empty spaces (as observed in the SEM images (Fig. 1)), in addition to the charge-transfer effect and the chemical reaction between the Si substrate and CeB_6 overlayer. The FOM_{SPP} (Fig. 8f) presented a peak at longer wavelengths than the FOM_{LSP}, which implies that SPP-based geometries (such as grating structures) are more suitable for targeting operation wavelengths in the MIR region.

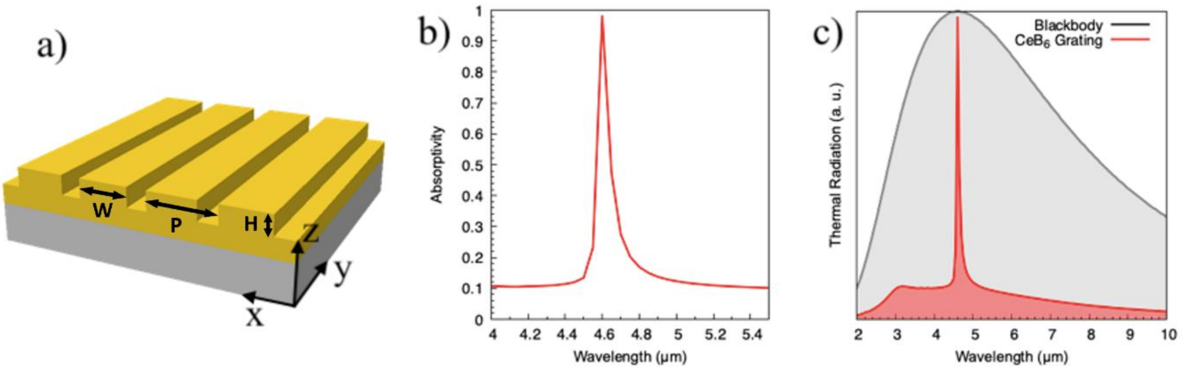

Fig. 9: (a) Schematic illustration of nanostructured plasmonic device; (b) simulation results of absorptivity and (c) wavelength-selective thermal emission of proposed device.

Fig. 9a shows the schematic illustration of a nanostructured thermal emitter device as a possible application of the obtained refractory plasmonic CeB_6 films. The design of the grating nanostructure (P = 4.55, W = 2.5, H = 0.25 μm) can be optimized via electromagnetic simulations aimed at plasmonic resonances in the MIR spectral region. Fig. 9b shows the optimized results for spectrally selective thermal emission at 4.6 μm, which corresponds to the vibrational frequency of the CO molecule. An absorptivity value extremely close to 1 was achieved, and the extremely narrow peak width with an FWHM of 90 nm resulted in Q-factor values exceeding 50. According to Kirchhoff's law for thermal radiation, absorptivity equals emissivity at thermal equilibrium. Therefore, the CeB_6-based grating perfect absorber can be used as a wavelength-selective perfect thermal emitter. Fig. 9c shows selective thermal emissions (red spectrum) based on the CeB_6 grating configuration for IR applications compared with the theoretical blackbody radiation at the temperature of 357 °C. At this temperature, the blackbody radiation peak is located at a wavelength of 4.6 μm, as determined by Wien's law. It should be noted that, in practical applications, the CeB_6-based device can be heated externally using a hot plate or internally through Joule heating. As a proof of concept, the proposed wavelength-selective thermal emitter efficiently generated mid-IR light at a specific wavelength of 4.6 μm. This shows that the favorable SPP response of the CeB_6 films, as shown in Fig. 8 (f), enables the fabrication of a high-resolution thermal emitter device, which can facilitate the development of high-temperature photothermal device technology in the MIR region.

CONCLUSIONS

The orientation and crystallinity of CeB_6 layers were strongly influenced by the template substrate and the deposition temperature of the film. Atomic surface rearrangement is determinant for the formation of epitaxial thin films, and the energy required for this rearrangement was primarily supplied via in-situ substrate heating. The XRD patterns and SEM observations showed that higher crystallinity was achieved at higher temperatures when for depositions on sapphire substrates, whereas Si substrates yielded inferior crystallinity above 800 °C. This temperature effect, in addition to the small lattice mismatch and symmetry matching between the CeB_6 overlayer and R-sapphire substrate, promoted the excellent epitaxial growth of CeB_6. Similar to previous studies regarding other metal hexaborides[37,43,44] a nearly commensurate relationship between the films and substrate promoted the epitaxial growth.

The plasmonic FOM_{LSP} of the CeB_6 thin films fabricated in this study achieve better performance in the 750–2000 nm range than other common refractory materials (W and Mo) with FOMs similar to that of Al (Fig. S5), which is one of the most widely used plasmonic materials (together with silver and gold). The plasmonic FOM_{SPP} of the CeB_6 thin films exhibited a peak in the MIR spectrum, thus indicating that SPP-based devices exhibit high performance in this wavelength region. In addition to the outstanding plasmonic response of CeB_6 in the IR region, its exceptionally high melting point above 2800 °C is noteworthy, as compared with that of conventional plasmonic coinage metals such as Al (300 °C for thin films and 660 °C for bulk), as well as its high resistance against oxidation up to approximately 800 °C in air. Therefore, CeB_6 is a robust candidate for high-temperature plasmonic photothermal applications, including spectroscopic thermal emitters for gas sensing, material-selective heating, and thermophotovoltaic devices.

ASSOCIATED CONTENT: Additional experimental (SEM, AFM, ellipsometry) and theoretical details (PDF)

ACKNOWLEDGMENTS:

This study was supported by the “Advanced Research Infrastructure for Materials and Nanotechnology in Japan (ARIM)” of the Ministry of Education, Culture, Sports, Science, and Technology (MEXT). DHP and TN were supported by KAKENHI Project 21F21370. The authors acknowledge Prof. S. Otani for the fruitful discussions.

REFERENCES

(1) Cahill, J. T.; Graeve, O. A. Hexaborides: A Review of Structure, Synthesis and Processing. *J. Mater. Res. Technol.* **2019**, *8* (6), 6321–6335. https://doi.org/10.1016/j.jmrt.2019.09.041.

(2) Chao, L.; Bao, L.; Wei, W.; Tegus, O. A Review of Recent Advances in Synthesis, Characterization and NIR Shielding Property of Nanocrystalline Rare-Earth Hexaborides and Tungsten Bronzes. *Sol. Energy* **2019**, *190*, 10–27. https://doi.org/10.1016/j.solener.2019.07.087.

(3) Mitterer, C. Borides in Thin Film Technology. *J. Solid State Chem.* **1997**, *133* (1), 279–291. https://doi.org/10.1006/jssc.1997.7456.

(4) Sani, E.; Sciti, D.; Failla, S.; Bellucci, A.; Mastellone, M.; Orlando, S.; Trucchi, D. M. Bulk Ceramics of Lanthanum Hexaboride with Enhanced Spectral Selectivity and Photothermal Efficiency for Novel Hybrid Thermal-Thermionic Solar Absorbers. *Sol. Energy* **2024**, *271*, 112423. https://doi.org/10.1016/j.solener.2024.112423.

(5) Akter, S.; Alaloul, M.; Odebowale, A. A.; Al Ani, I.; As’Ham, K.; Abdo, S.; Hattori, H. T. Near-Ultraviolet Photodetector Using Cerium Hexaboride Alloy. *J. Mod. Opt.* **2024**, *71* (1–3), 25–33. https://doi.org/10.1080/09500340.2024.2390606.

(6) Johnson, R. W.; Daane, A. H. Electron Requirements of Bonds in Metal Borides. *J. Chem. Phys.* **1963**, *38* (2), 425–432. https://doi.org/10.1063/1.1733675.

(7) Longuet-Higgins. The Electronic Structure of the Borides *M* B$_6$. *Proc. R. Soc. Lond. Ser. Math. Phys. Sci.* **1954**, *224* (1158), 336–347. https://doi.org/10.1098/rspa.1954.0162.

(8) Etourneau, J.; Mercurio, J.-P.; Hagenmuller, P. Compounds Based on Octahedral B6 Units: Hexaborides and Tetraborides. In *Boron and Refractory Borides*; Matkovich, V. I., Ed.; Springer Berlin Heidelberg: Berlin, Heidelberg, 1977; pp 115–138. https://doi.org/10.1007/978-3-642-66620-9_10.

(9) Mercurio, J. P.; Etourneau, J.; Naslain, R.; Hagenmuller, P. Electrical and Magnetic Properties of Some Rare-Earth Hexaborides. *J. Common Met.* **1976**, *47*, 175–180. https://doi.org/10.1016/0022-5088(76)90093-X.

(10) Kuzanyan, A. A.; Kuzanyan, A. S.; Petrosyan, S. I.; Kuzanyan, V. S.; Badalyan, G. R. Electron Beam Deposition of Lanthanum Hexaboride Films for Usage as Anti-Reflective Coating. *J. Contemp. Phys. Armen. Acad. Sci.* **2020**, *55* (2), 164–170. https://doi.org/10.3103/S1068337220020073.

(11) Mattox, T. M.; Urban, J. J. Tuning the Surface Plasmon Resonance of Lanthanum Hexaboride to Absorb Solar Heat: A Review. *Materials* **2018**, *11* (12), 2473. https://doi.org/10.3390/ma11122473.

(12) Zimmer, C. M.; Yoganathan, K.; Giebel, F. J.; Lutzenkirchen-Hecht, D.; Glosekotter, P.; Kallis, K. T. Photoemission Properties of LaB6 Thin Films for the Use in PIDs. In *14th IEEE International*

Conference on Nanotechnology; IEEE: Toronto, ON, Canada, 2014; pp 877–881. https://doi.org/10.1109/NANO.2014.6967988.

(13) Zhang, H.; Jimbo, Y.; Niwata, A.; Ikeda, A.; Yasuhara, A.; Ovidiu, C.; Kimoto, K.; Kasaya, T.; Miyazaki, H. T.; Tsujii, N.; Wang, H.; Yamauchi, Y.; Fujita, D.; Kitamura, S.; Manabe, H. High-Endurance Micro-Engineered LaB6 Nanowire Electron Source for High-Resolution Electron Microscopy. *Nat. Nanotechnol.* **2022**, *17* (1), 21–26. https://doi.org/10.1038/s41565-021-00999-w.

(14) Xiao, Y.; Zhang, X.; Liu, H.; Zhang, J. Preparation and Field Emission Properties of Single-Crystal CeB6 Tips. *J. Electron. Mater.* **2020**, *49* (1), 485–492. https://doi.org/10.1007/s11664-019-07723-4.

(15) Shishido, H.; Kawai, K.; Futagami, A.; Noguchi, S.; Ishida, T. Thin Film Growth of Rare-Earth Hexaboride. In *Proceedings of the International Conference on Strongly Correlated Electron Systems (SCES2013)*; Journal of the Physical Society of Japan: Tokyo, Japan, 2014. https://doi.org/10.7566/JPSCP.3.011045.

(16) Hatanaka, D.; Asanuma, E.; Takeda, K.; Ikeda, T.; Nakamura, M.; Nakanishi, Y.; Iga, F.; Harada, Y.; Yamaguchi, H.; Yoshizawa, M. Synthesis and Characterization of Rare-Earth Boride Thin Films of CeB $_6$ Fabricated by MBE Method. In *Proceedings of the International Conference on Strongly Correlated Electron Systems (SCES2013)*; Journal of the Physical Society of Japan: Tokyo, Japan, 2014. https://doi.org/10.7566/JPSCP.3.011049.

(17) Xu, J. Q.; Mori, T.; Bando, Y.; Golberg, D.; Berthebaud, D.; Prytuliak, A. Synthesis of CeB6 Thin Films by Physical Vapor Deposition and Their Field Emission Investigations. *Mater. Sci. Eng. B* **2012**, *177* (1), 117–120. https://doi.org/10.1016/j.mseb.2011.09.038.

(18) Ngo, T. D.; Tran, T. P.; Ngo, H. D.; Nagao, T. A Simultaneous Material-Device Optimization for Plasmonic Devices: A Combined Ab Initio and Electromagnetic Simulation for Photothermal Transducers. *Adv. Opt. Mater.* **2022**, *10* (23), 2201320. https://doi.org/10.1002/adom.202201320.

(19) Tran, P. T.; Ngo, T. D.; Ngo, H. D.; Handegård, Ø. S.; Nagao, T. Metal-Insulator-Metal Strip Spectroscopic Infrared Photothermal Absorber Based on Uniaxially Oriented Plasmonic Lanthanum Hexaboride Films. *Opt. Express* **2022**, *30* (21), 38630. https://doi.org/10.1364/OE.463522.

(20) Sugavaneshwar, R. P.; Handegård, Ø. S.; Doan, A. T.; Ngo, T. D.; Tran, T. P.; Ngo, H. D.; Dao, T. D.; Ishii, S.; Otani, S.; Nagao, T. Optical Properties and Optimization of LaB$_6$ Thin Films for Photothermal Applications. *Adv. Opt. Mater.* **2022**, *10* (8), 2101787. https://doi.org/10.1002/adom.202101787.

(21) Giannozzi, P.; Baroni, S.; Bonini, N.; Calandra, M.; Car, R.; Cavazzoni, C.; Ceresoli, D.; Chiarotti, G. L.; Cococcioni, M.; Dabo, I.; Dal Corso, A.; De Gironcoli, S.; Fabris, S.; Fratesi, G.; Gebauer, R.; Gerstmann, U.; Gougoussis, C.; Kokalj, A.; Lazzeri, M.; Martin-Samos, L.; Marzari, N.; Mauri, F.; Mazzarello, R.; Paolini, S.; Pasquarello, A.; Paulatto, L.; Sbraccia, C.; Scandolo, S.; Sclauzero, G.; Seitsonen, A. P.; Smogunov, A.; Umari, P.; Wentzcovitch, R. M. QUANTUM ESPRESSO: A Modular and Open-Source Software Project for Quantum Simulations of Materials. *J. Phys. Condens. Matter* **2009**, *21* (39), 395502. https://doi.org/10.1088/0953-8984/21/39/395502.

(22) Giannozzi, P.; Andreussi, O.; Brumme, T.; Bunau, O.; Buongiorno Nardelli, M.; Calandra, M.; Car, R.; Cavazzoni, C.; Ceresoli, D.; Cococcioni, M.; Colonna, N.; Carnimeo, I.; Dal Corso, A.; De Gironcoli, S.; Delugas, P.; DiStasio, R. A.; Ferretti, A.; Floris, A.; Fratesi, G.; Fugallo, G.; Gebauer, R.; Gerstmann, U.; Giustino, F.; Gorni, T.; Jia, J.; Kawamura, M.; Ko, H.-Y.; Kokalj, A.; Küçükbenli, E.; Lazzeri, M.; Marsili, M.; Marzari, N.; Mauri, F.; Nguyen, N. L.; Nguyen, H.-V.; Otero-de-la-Roza, A.; Paulatto, L.; Poncé, S.; Rocca, D.; Sabatini, R.; Santra, B.; Schlipf, M.; Seitsonen, A. P.; Smogunov, A.; Timrov, I.; Thonhauser, T.; Umari, P.; Vast, N.; Wu, X.; Baroni, S. Advanced Capabilities for Materials Modelling with Quantum ESPRESSO. *J. Phys. Condens. Matter* **2017**, *29* (46), 465901. https://doi.org/10.1088/1361-648X/aa8f79.

(23) Vanderbilt, D. Soft Self-Consistent Pseudopotentials in a Generalized Eigenvalue Formalism. *Phys. Rev. B* **1990**, *41* (11), 7892–7895. https://doi.org/10.1103/PhysRevB.41.7892.

(24) Quantum ESPRESSO Http://Www.Quantum-Espresso.Org.

(25) Perdew, J. P.; Burke, K.; Ernzerhof, M. Generalized Gradient Approximation Made Simple. *Phys. Rev. Lett.* **1996**, *77* (18), 3865–3868. https://doi.org/10.1103/PhysRevLett.77.3865.

(26) Monkhorst, H. J.; Pack, J. D. Special Points for Brillouin-Zone Integrations. *Phys. Rev. B* **1976**, *13* (12), 5188–5192. https://doi.org/10.1103/PhysRevB.13.5188.

(27) Foroozani, N.; Lim, J.; Fabbris, G.; Rosa, P. F. S.; Fisk, Z.; Schilling, J. S. Suppression of Dense Kondo State in CeB6 under Pressure. *Phys. B Condens. Matter* **2015**, *457*, 12–16. https://doi.org/10.1016/j.physb.2014.10.001.

(28) Srikant, V.; Sergo, V.; Clarke, D. R. Epitaxial Aluminum-Doped Zinc Oxide Thin Films on Sapphire: I, Effect of Substrate Orientation. *J. Am. Ceram. Soc.* **1995**, *78* (7), 1931–1934. https://doi.org/10.1111/j.1151-2916.1995.tb08912.x.

(29) Kojima, K.; Ohbayashi, K.; Hihara, T.; Kunii, S.; Komatsubara, T.; Kasuya, T. Raman Scattering in CeB6. *Phys. Lett. A* **1979**, *72* (1), 51–52. https://doi.org/10.1016/0375-9601(79)90524-3.

(30) Ogita, N.; Nagai, S.; Okamoto, N.; Udagawa, M.; Iga, F.; Sera, M.; Akimitsu, J.; Kunii, S. Raman Scattering Investigation of R B 6 (R = Ca , La, Ce, Pr, Sm, Gd, Dy, and Yb). *Phys. Rev. B* **2003**, *68* (22), 224305. https://doi.org/10.1103/PhysRevB.68.224305.

(31) Ishii, M.; Aono, M.; Muranaka, S.; Kawai, S. RAMAN SPECTRA OF METALLIC AND SEMICONDUCTING METAL HEXABORIDES (MBs).

(32) Groome, C.; Roh, I.; Mattox, T. M.; Urban, J. J. Effects of Size and Structural Defects on the Vibrational Properties of Lanthanum Hexaboride Nanocrystals. *ACS Omega* **2017**, *2* (5), 2248–2254. https://doi.org/10.1021/acsomega.7b00263.

(33) Ishii, M.; Tanaka, T.; Bannai, E.; Kawai, S. Raman Scattering in Metallic LaB $_6$. *J. Phys. Soc. Jpn.* **1976**, *41* (3), 1075–1076. https://doi.org/10.1143/JPSJ.41.1075.

(34) Tadaaki, N.; Kazuo, K.; Yoshitaka, I.; Chuhei, O.; Otani, S. Surface Phonons of LaB6(100): Deformation of Boron Octahedra at the Surface. *Surf. Sci.* **1993**, *290* (3), 436–444. https://doi.org/10.1016/0039-6028(93)90726-Z.

(35) Waldhauser, W.; Mitterer, C.; Laimer, J.; Störi, H. Sputtered Thermionic Hexaboride Coatings. *Surf. Coat. Technol.* **1998**, *98* (1–3), 1315–1323. https://doi.org/10.1016/S0257-8972(97)00263-6.

(36) Handegard, O. Covalent and Semicovalent Non-Metal Plasmonic Materials for Interfacial Photo-Energy Conversion, Hokkaido University, 2020.

(37) Handegård, Ø. S.; Ngo, H. D.; Sugavaneshwar, R. P.; Doan, T. A.; Naoki, F.; Otani, S.; Nagao, T. Epitaxial Growth Mechanism of High-Crystallinity Lanthanum Hexaboride (001) Thin Films on Silicon (001) by Electron Beam Deposition. *Appl. Phys. Express* **2020**, *13* (5), 055504. https://doi.org/10.35848/1882-0786/ab8728.

(38) Dušek, M.; Petříček, V.; Wunschel, M.; Dinnebier, R. E.; van Smaalen, S. Refinement of Modulated Structures against X-Ray Powder Diffraction Data with *JANA* 2000. *J. Appl. Crystallogr.* **2001**, *34* (3), 398–404. https://doi.org/10.1107/S0021889801003302.

(39) Makita, R.; Tanaka, K.; Ōnuki, Y. 5 *d* and 4 *f* Electron Configuration of CeB $_6$ at 340 and 535 K. *Acta Crystallogr. B* **2008**, *64* (5), 534–549. https://doi.org/10.1107/S0108768108026542.

(40) Wu, Z. J.; Su, Z. M. Electronic Structures and Chemical Bonding in Transition Metal Monosilicides MSi (M=3d, 4d, 5d Elements). *J. Chem. Phys.* **2006**, *124* (18), 184306. https://doi.org/10.1063/1.2196040.

(41) Horn-von Hoegen, M.; Copel, M.; Tsang, J. C.; Reuter, M. C.; Tromp, R. M. Surfactant-Mediated Growth of Ge on Si(111). *Phys. Rev. B* **1994**, *50* (15), 10811–10822. https://doi.org/10.1103/PhysRevB.50.10811.

(42) Fujikawa, Y.; Akiyama, K.; Nagao, T.; Sakurai, T.; Lagally, M. G.; Hashimoto, T.; Morikawa, Y.; Terakura, K. Origin of the Stability of Ge(105) on Si: A New Structure Model and Surface Strain

Relaxation. *Phys. Rev. Lett.* **2002**, *88* (17), 176101. https://doi.org/10.1103/PhysRevLett.88.176101.

(43) Roucka, R.; Tolle, J.; Chizmeshya, A. V. G.; Tsong, I. S. T.; Kouvetakis, J. Epitaxial Film Growth of Zirconium Diboride on Si(001). *J. Cryst. Growth* **2005**, *277* (1–4), 364–371. https://doi.org/10.1016/j.jcrysgro.2005.01.080.

(44) Li, Y.; Ma, Q.; Huang, S. X.; Chien, C. L. Thin Films of Topological Kondo Insulator Candidate SmB $_6$: Strong Spin-Orbit Torque without Exclusive Surface Conduction. *Sci. Adv.* **2018**, *4* (1), eaap8294. https://doi.org/10.1126/sciadv.aap8294.